cal, can be drawn in the three-dimensional case [using, for example, the formalism developed by Navaza & Silva (1979)].

These conclusions do not mean that $\langle \hat{m} \rangle_{ME}$ is equivalent to the traditional inverse Fourier reconstruction τ (when phases are available), because τ is not x, even if they have the same number of terms corresponding to the same reciprocal vectors. It just clarifies the sense of super-resolution and puts limits to the confidence we can give to phases and Fourier coefficients estimated by any local MEM procedure that only uses experimental data as constraints.

References

ALZARI, P. & NAVAZA, J. (1983). Unpublished work.

BRICOGNE, G. (1984). *Acta Cryst.* A**40**, 410-445.

COLLINS, D. M. (1982). *Nature (London)*, **298**, 49-51.

DE TITTA, G. T., LANGS, D. A., EDMONDS, J. W. & DUAX, W. L. (1980). *Acta Cryst.* B**36**, 638-645.

HULL, S. E., LEBAN, I., MAIN, P., WHITE, P. S. & WOOLFSON, M. M. (1976). *Acta Cryst.* B**32**, 2374-2381.

JAYNES, E. T. (1957). *Phys. Rev.* **106**, 620-630.

JAYNES, E. T. (1968). *IEEE Trans. Syst. Sci. Cybern.* **SSC-4**, 227-241.

JONES, P. G., SHELDRICK, G. M., GLUSENKAMP, K. H. & TIETZE, L. F. (1980). *Acta Cryst.* B**36**, 481-483.

KUBO, R., ICHIMURA, H., USUI, T. & HASHITSUME, N. (1978). *Statistical Mechanics.* Amsterdam: North-Holland.

LIVESEY, A. K. & SKILLING, J. (1985). *Acta Cryst.* A**41**, 113-122.

NAVAZA, J. (1985). *Acta Cryst.* A**41**, 232-244.

NAVAZA, J., CASTELLANO, E. E. & TSOUCARIS, G. (1983). *Acta Cryst.* A**39**, 622-631.

NAVAZA, J. & SILVA, A. M. (1979). *Acta Cryst.* A**35**, 266-275.

RANGO, C. DE & NAVAZA, J. (1984). Nato Workshop. Future Direct Methods, Orsay, April 1984.

SEMENOVSKAYA, S. V., KHACHATURYAN, K. A. & KHACHATURYAN, A. G. (1985). *Acta Cryst.* A**41**, 268-273.

SHANNON, C. E. & WEAVER, W. (1949). *The Mathematical Theory of Communication.* Univ. of Illinois Press.

SMITH, G. D. (undated). Medical Foundation of Buffalo. Unpublished.

Acta Cryst. (1986). A**42**, 223-230

An Examination of the Relationship of the $\Delta\omega, \Delta 2\theta$ Intensity Distribution to Crystal Substructure (Mosaic Distribution) and Shape

BY A. MCL. MATHIESON AND A. W. STEVENSON

Division of Chemical Physics, CSIRO, PO Box 160, *Clayton, Victoria, Australia* 3168

(*Received* 19 *February* 1985; *accepted* 20 *December* 1985)

Abstract

The basic $\Delta\omega, \Delta 2\theta$ technique for examining single-crystal Bragg reflections [Mathieson (1982). *Acta Cryst.* A**38**, 378-387] has recently been improved [Mathieson & Stevenson (1984). *Aust. J. Phys.* **37**, 657-665], by using a simple experimental modification which reduces the source component to a minor (angular) role, thereby making the extraction (deconvolution) of the remaining components more accurate. The application of this new technique in the determination of reflectivity (rocking) curves for imperfect crystals has been demonstrated [Mathieson & Stevenson (1985). *Acta Cryst.* A**41**, 290-296]. In the present case, the examination of individual reflections from a small single crystal of $CuInSe_2$ reveals that the improved technique is capable (i) of identifying, by its locus extension in $\Delta\omega, \Delta 2\theta$ space, diffraction from one side of the specimen crystal to the other (in the diffraction plane), even for a crystal of average dimension $\sim$0·06 mm, and (ii) of estimating the reflectivity curve for different parts of the crystal. A series of model cases is discussed, to clarify the interpretation of observed two-dimensional intensity distributions. While considered here in relation to a small crystal, this technique is applicable to extended-plate crystals (in transmission mode) by a selected-area procedure.

1. Introduction

In a recent series of papers, Mathieson (1982) being the first, Mathieson has demonstrated the advantages of the two-dimensional $\Delta\omega, \Delta 2\theta$ method for examining single-crystal Bragg reflections, relative to the conventional $\Delta\omega$ profile method. The one-dimensional intensity profile obtained in the conventional procedure represents the convolution of a number of components such as the mosaic spread, μ, the source size, σ, the wavelength distribution, λ, the specimen crystal size (Mathieson, 1984*a*), c, and, most importantly, the wide aperture in front of the detector, A. The $\Delta\omega, \Delta 2\theta$ technique, involving the introduction of a narrow aperture in front of the detector and the consequent extension to a second measurement parameter, results, in effect, in a form of partial deconvolution, with the individual major components being readily identified by their characteristic loci in $\Delta\omega, \Delta 2\theta$ space.

0108-7673/86/040223-08$01.50

The principal component distributions in $\Delta\omega$, $\Delta 2\theta$ space are, generally, μ, σ and λ. Mathieson & Stevenson (1984) have demonstrated, by way of a simple experimental modification, that the σ component can be reduced to a minor (angular) role. The remaining principal components, μ and λ, can then be determined with considerable accuracy. The specimen-specific distribution μ is the component of greatest physical significance because of its identification with the reflectivity distribution, r, of the individual Bragg reflection in question, and hence with the variation of extinction within that reflection (Mathieson, 1984*b*).

Mathieson & Stevenson (1985) have applied the improved $\Delta\omega$, $\Delta 2\theta$ technique in the determination of a particular reflectivity curve for an imperfect single crystal of tetragonal $CuInSe_2$, of average dimension ~0·06 mm. In that study, the two-dimensional array of data points for the $\bar{1}\bar{1}2$ reflection, collected as an ω scan using unfiltered Mo $K\alpha$ radiation, was transformed in such a way that the μ/r and λ components, the only major components present, were at right angles. [The use of affine transformations parallel to either the $\Delta 2\theta$ axis (notation: $s = n$) or the $\Delta\omega$ axis (notation: $t = n$) has been discussed in detail by Mathieson & Stevenson (1985).] Then, under the assumptions that the mosaic distribution of the specimen crystal was homogeneous and the distribution centres were parallel along the crystal (in the diffraction plane), the data points were summed parallel to λ, to yield $r(\Delta\omega)$, or more precisely $r^*(\Delta\omega)$, the extinguished reflectivity distribution (see Mathieson, 1984*b*). In the case of the reflection considered, $\bar{1}\bar{1}2$, the assumptions made in regard to the mosaic distribution appear to be quite justifiable [see, for example, Fig. 2(*b*) of Mathieson & Stevenson (1984) or Fig. 3 of Mathieson & Stevenson (1985)]. In order to demonstrate this point further, Fig. 1(*a*) shows a series of slice scans (Mathieson, 1982) taken along the λ component, each parallel to the μ^*/r^* component. The data for each curve have been put on a common scale and plotted with a displacement along the vertical axis, for ease of comparison. The shapes of the curves are remarkably similar and the systematic movement of the peak position in $\Delta\omega$ is very slight.

In cases where the $CuInSe_2$ crystal being considered here is in other orientations relative to the incident X-ray beam, be it a reflection other than the $\bar{1}\bar{1}2$ or a different azimuthal position about the $\bar{1}\bar{1}2$ scattering vector, the mosaic distribution in the diffraction plane may not be homogeneous and/or the distribution centres may not be parallel along the crystal. The (extinguished) reflectivity distribution would not then be invariant along the λ axis of the corresponding intensity distribution, $I(\Delta\omega, \Delta 2\theta)$, and the result of summing data points parallel to λ would be an 'averaged' r^* distribution. An example of such a case is given in Fig. 1(*b*), for the $\bar{1}\bar{1}\bar{2}$ reflection at an azimuthal angle, ψ, of 100°. Fig. 1(*b*) was derived in an analogous manner to Fig. 1(*a*). In this case, μ^* is not homogeneous and the distribution centres are not parallel. Interpretation of Fig. 1(*b*) will be expounded later in the paper.

2. Relationship of the $\Delta\omega$, $\Delta 2\theta$ distribution to crystal substructure (mosaic distribution) and shape

The experimental investigations that have provided insight into the relationship of $I(\Delta\omega, \Delta 2\theta)$ to crystal substructure and shape were carried out on the {112} reflections of the $CuInSe_2$ crystal used by Mathieson & Stevenson (1984, 1985), by applying the improved $\Delta\omega$, $\Delta 2\theta$ technique with unfiltered Mo $K\alpha$ radiation. This small imperfect single crystal has an irregular shape with an average dimension ~0·06 mm. $CuInSe_2$ is tetragonal and has the chalcopyrite structure (Parkes, Tomlinson & Hampshire, 1973). The {112} reflections were chosen for study because they are intense and low angle ($\theta \sim 6{\cdot}1°$).

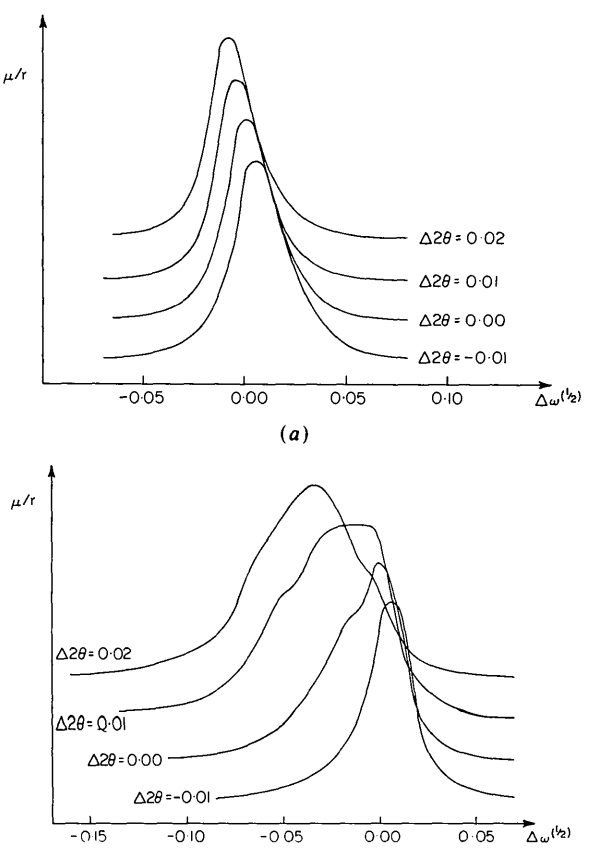

Fig. 1. Series of slice scans taken along the λ component, each parallel to the μ/r component for (*a*) the $\bar{1}\bar{1}2$ reflection at $\psi = 0°$ and (*b*) the $\bar{1}\bar{1}\bar{2}$ reflection at $\psi = 100°$. For ease of comparison, each curve has been displaced along the vertical axis, the data for each curve having already been put on a common scale (by making peak intensities agree).

Initially, this investigation involved recording the $I(\Delta\omega, \Delta 2\theta)$ distributions for the $\bar{1}1\bar{2}$ reflection in the -2θ region and its Friedel-pair reflection, $1\bar{1}2$, in the $+2\theta$ region, *i.e.* retaining essentially the same orientation of the specimen crystal to the incident X-ray beam and simply traversing from -2θ to $+2\theta$ and $-\omega$ to $+\omega$. These distributions are shown in Fig. 2, in the correct mutual disposition relative to the origin of the Ewald circle, *O*. The similarity in detail of the two distributions is such as to leave little doubt that they are due to the diffracting characteristics of the specimen crystal as it is presented to the incident beam. This is confirmed by other such pairs of $I(\Delta\omega, \Delta 2\theta)$ distributions, some of which are particularly distinctive, a consequence of the *local* mosaic distributions (as discussed later).

The next step in this investigation involved comparison of the $I(\Delta\omega, \Delta 2\theta)$ distributions of the $\bar{1}\bar{1}\bar{2}$ reflection in the $+2\theta$ region for $\psi = 100$ and $\psi = 280°$. The two results are shown in Figs. 3(*a*) (i) and (ii) respectively. While obviously related by a sort of 'mirroring' across the $\Delta 2\theta$ axis, the precise relationship is somewhat obscured because the direction of the λ locus is such that it 'distorts' the two distributions differently, remembering that $I(\Delta\omega, \Delta 2\theta)$ represents the convolution of μ, λ and the residual resolution function $R(\Delta\omega, \Delta 2\theta)$ (Mathieson & Stevenson, 1984, 1985). When one applies an affine transformation of the type $t = \frac{1}{2}$ (see Mathieson & Stevenson, 1985), the results for the two $I(\Delta\omega, \Delta 2\theta)$ distributions are as shown in Figs. 3(*b*) (i) and (ii) respectively. Presented in this way, the 'mirror' relationship associated with the 180° rotation around the pole (scattering vector) is evident.

With these data, it is possible to deduce the significance of the intensity distribution detail in terms of certain physical features, *i.e.* the *local* mosaic spread of the specimen crystal. To arrive at an explanation in this particular case, it is useful to develop the relationship between the $I(\Delta\omega, \Delta 2\theta)$ distribution and the crystal shape and mosaic spread, starting from that of a small single crystal with zero mosaic spread. In this way, we can establish the relationship for a range of cases and develop an interpretation for intensity distributions arising from specimen crystals with other, different, characteristics.

We shall consider the situation for a low-angle reflection, where the locus associated with the crystal size, *c*, is close to the λ locus (see Mathieson, 1984*a*). [In the present case, for the {112} reflections and allowing for unequal source-to-crystal (*S*) and crystal-to-detector (*D*) distances, the loci for *c* and λ will be separated by ~2°, for the ω-scan mode ($s = 0$).] For this modelling exercise, we assume the λ distribution to be sharply monochromatic. Only the ω-scan mode ($s = 0$) will be treated here, readers can readily deduce the results for other scan modes and for other regions of θ by consulting Mathieson & Stevenson (1985) and Mathieson (1984*a*), respectively.

The basic features of the experiment are shown in Fig. 4(*a*). The ends of the crystal are *a* and *b*, *c* identifying its centre. The diffraction from these different parts of the crystal are therefore identified by *a*, *b* and *c*, so that the size of the range along $\Delta 2\theta$, *i.e.* *ACB*, provides an estimate of the size of the crystal.

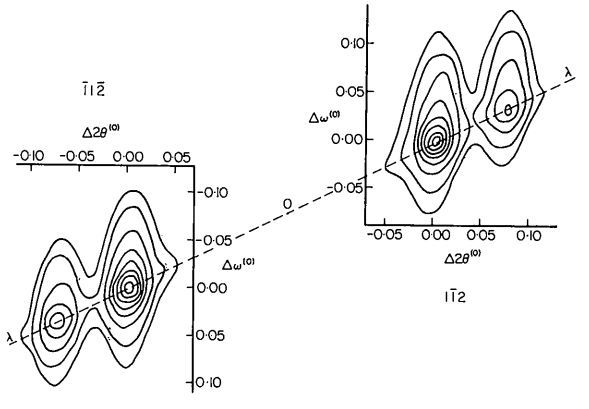

Fig. 2. The $I(\Delta\omega, \Delta 2\theta)$ distributions ($s = 0$) for the $\bar{1}1\bar{2}$ reflection in the -2θ region and its Friedel-pair reflection, $1\bar{1}2$, in the $+2\theta$ region, in the correct mutual disposition relative to the origin of the Ewald circle, *O*. The contour levels are 3000, 2500, 2000, 1500, 1000, 500, 200 and 100 counts s^{-1}.

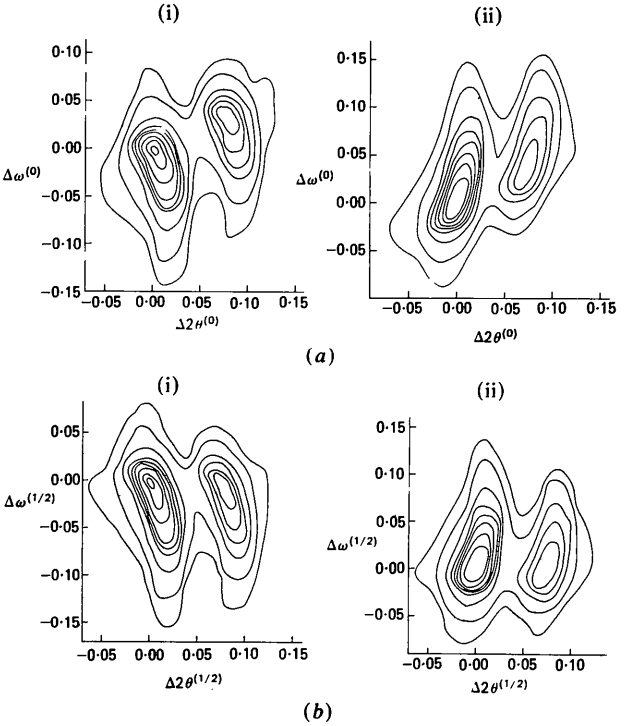

Fig. 3. (*a*) The $I(\Delta\omega, \Delta 2\theta)$ distributions ($s = 0$) for the $\bar{1}\bar{1}\bar{2}$ reflection in the $+2\theta$ region for (i) $\psi = 100°$ and (ii) $\psi = 280°$. The contour levels are 5000, 4000, 3000, 2000, 1500, 1000, 500, 200 and 100 counts s^{-1} for (i) and the same as in Fig. 2 for (ii). (*b*) The $I(\Delta\omega, \Delta 2\theta)$ distributions for the data presented in (*a*) after a $t = 1/2$ affine transformation has been carried out, (i) for $\psi = 100°$ and (ii) for $\psi = 280°$.

The dimension of the source, S, in the diffraction plane, h [see Fig. 4(b)], is much smaller than for the conventional X-ray tube orientation (Mathieson & Stevenson, 1984). It should be noted that, as the mosaic fan, at 'a' (say), passes over the source, S, diffraction from a only occurs along the path SaA, *i.e.* the position a is identified as associated with the position A in the $\Delta 2\theta$ dimension. It should also be noted that the points A, B and C do not rotate about c as the crystal rotates, but are fixed in $\Delta 2\theta$. Fig. 4(b) presents a magnified version of the path SaA, indicating the angular dimension of the $\Delta\omega$ component of the resolution function, $R(\Delta\omega, \Delta 2\theta)$. For comparative purposes, the sizes of the mosaic spread and the source illumination are indicated in Figs. 4(a) and (b) respectively.

Fig. 5(a) depicts the mosaic spread at the three points a, c and b (refer to Fig. 4) for a variety of cases. The size of the mosaic spread is indicated diagrammatically by the size of the fan at a given point, and the relative orientations of the fans by their centre (peak) lines. Fig. 5(b) shows, in each case, the corresponding $I(\Delta\omega, \Delta 2\theta)$ distribution, pp indicating the peak of the distribution. In this manner we can demonstrate the effects of inhomogeneity and asymmetry in the mosaic spread, as well as the effects of the distribution (fan) centres not being parallel, along the crystal. We now discuss the individual cases depicted in Fig. 5.

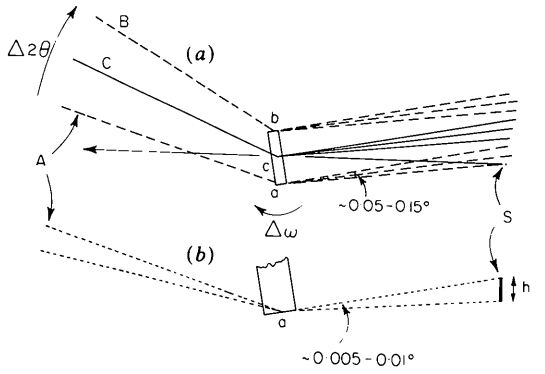

Fig. 4. (a) The basic experimental set-up, consisting of the source S, the specimen crystal (ends denoted by a and b, and centre by c) and the detector (not drawn) to intercept the diffracted radiation. Mosaic fans are depicted at positions a, c and b along the crystal. (b) A magnified version of the path SaA. These diagrams are not, of course, to scale.

For a crystal with zero mosaic spread and parallel peak lines, Fig. 5(a)(i), the corresponding $I(\Delta\omega, \Delta 2\theta)$ distribution is shown in Fig. 5(b)(i), the locus being at a slope of $\sim\tan^{-1}\frac{1}{2}$ to the $\Delta 2\theta$ axis (see earlier in this section). Next, we consider the case of a crystal of the same size but with a homogeneous mosaic spread of significant magnitude, the mosaic spread being either symmetrical (full lines) or asymmetrical (dashed lines) along the crystal and with the centre lines of the fans being parallel, Fig. 5(a)(ii). The corresponding $I(\Delta\omega, \Delta 2\theta)$ distributions are shown in Fig. 5(b)(ii). If the centres are parallel but the mosaic spread is not homogeneous along the crystal, for example Figs. 5(a)(iii) and (iv), then the corresponding $I(\Delta\omega, \Delta 2\theta)$ distributions are as shown in Figs. 5(b)(iii) and (iv). When the mosaic distribution centres are non-parallel but point to one centre and the mosaic spread is homogeneous (full lines) or changing linearly from a to b (dashed lines), Fig. 5(a)(v), the corresponding $I(\Delta\omega, \Delta 2\theta)$ distributions are as shown in Fig. 5(b)(v). Figs. 5(a)(vi) and (b)(vi) correspond to the case of a 180° rotation in ψ relative to the case depicted in Figs. 5(a)(v) and (b)(v). It should be noted that the slope of the line pp depends upon the radius of curvature for the mosaic distribution centres. When the centres are

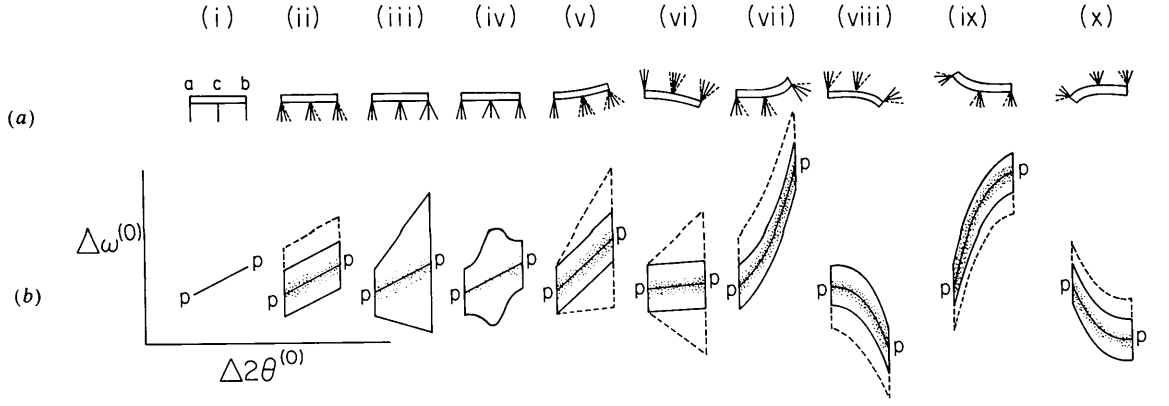

Fig. 5. (a) The mosaic spread at points a, c and b along the crystal for a variety of cases [(i)-(x)]. (b) The corresponding $I(\Delta\omega, \Delta 2\theta)$ distributions ($s=0$), pp indicating the peak of the distribution. It should be noted that the extents of these distributions along $\Delta\omega$ and $\Delta 2\theta$ are not to scale. For instance, the height ($\Delta\omega$), associated with mosaic spread, is typically ~0·05-0·15° [as indicated in Fig. 4(a)] in the present case, whereas the width ($\Delta 2\theta$), associated with crystal size, is typically ~0·03°. It should also be noted that while the crystal has been pictured as being curved (bent) in (a)(v)-(x), the associated mosaic spreads along the crystal (and in particular their relative orientations) might just as easily accompany a macroscopically 'straight' crystal.

non-parallel and the effective curvature increases (or the effective radius of curvature decreases) from *a* to *b* (full lines for symmetrical mosaic spread and dashed for asymmetrical mosaic spread), Fig. 5(*a*)(vii), the corresponding $I(\Delta\omega, \Delta 2\theta)$ distributions are as shown in Fig. 5(*b*)(vii). Figs. 5(*a*)(viii) and (*b*)(viii) correspond to the case of a 180° rotation in ψ relative to the case depicted in Figs. 5(*a*)(vii) and (*b*)(vii). The line *pp* is now curved. Finally, Figs. 5(*a*)(ix) and (x) are analogous to Figs. 5(*a*)(vii) and (viii) respectively, but the effective curvature decreases, rather than increases, from *a* to *b*. The corresponding $I(\Delta\omega, \Delta 2\theta)$ distributions are shown in Figs. 5(*b*)(ix) and (x).

The above discussion is for a reflection involving a crystal of uniform cross section. If the cross section varies, this will affect the magnitude of the diffracted intensity from specific points in the specimen crystal, with appropriate effects for the local absorption and extinction.

The experimental results for the $\bar{1}\bar{1}2$ reflection of $CuInSe_2$, Figs. 3(*a*)(i) and (ii), accord, in terms of the general distribution, with Figs. 5(*b*)(viii) and (vii) respectively. Thus we see that the effect, on the $I(\Delta\omega, \Delta 2\theta)$ distribution, of rotating the specimen crystal by 180° in ψ is in accord with the model used. While the effects of non-parallel mosaic distribution centres and asymmetry of the local mosaic spreads along the crystal are quite apparent in Figs. 3(*a*)(i) and (ii), the effect of inhomogeneity in the mosaic spread along the crystal may not be so obvious and, indeed, Figs. 5(*a*)(vii) and (viii) depict a homogeneous mosaic spread. In Fig. 1(*b*), presented in § 1, which utilized the data in Fig. 3(*a*)(i) [or more precisely Fig. 3(*b*)(i)], the effects of non-parallel centres and asymmetric mosaic spreads along the crystal are obvious. It is also apparent that the mosaic spread along the crystal is inhomogeneous, with the distribution at the *a* end of the crystal much narrower than that at the *b* end. Indeed, the slice scan at $\Delta 2\theta = -0{\cdot}01°$ is very similar to those slice scans presented in Fig. 1(*a*). The other slice scans ($\Delta 2\theta = 0{\cdot}00$, 0·01 and 0·02°) may be revealing some evidence of fragmentation (*cf.* Mathieson, 1982).

The 'mirror' relationship observed earlier, between Figs. 3(*b*)(i) and (ii), and associated with the 180° rotation in ψ, can now be readily understood from Fig. 5. It must be remembered that the $I(\Delta\omega, \Delta 2\theta)$ distributions in Fig. 5(*b*) are for the $s = 0$ (ω) scan mode, and so we need to visualize the effect of a $t = \frac{1}{2}$ affine transformation, *e.g.* the lines *pp* in Figs. 5(*b*)(i)–(iv) would be very nearly horizontal, rather than at $\sim\tan^{-1}\frac{1}{2}$ to the $\Delta 2\theta$ axis. Comparison of Figs. 5(*b*)(v) with (vi), (vii) with (viii) and (ix) with (x), after such a transformation has been made, clearly reveals this 'mirror' relationship.

Fig. 6 shows the $I(\Delta\omega, \Delta 2\theta)$ distribution obtained in the -2θ region for the 112 reflection in a particular asymmetric position ($\psi \neq 0$ or 180°, $\omega \neq \theta$). The specimen crystal was initially in the orientation to obtain Fig. 3(*a*)(i), then $+2\theta$ was changed to -2θ and $+\omega$ to $+\omega - 2\theta$. This procedure was used, for a different reflection (in a symmetric position), in Fig. 2, and the comparison of Figs. 3(*a*)(i) and 6 confirms the earlier conclusions, *i.e.* the similarity in detail of the two $I(\Delta\omega, \Delta 2\theta)$ distributions is due to the diffracting characteristics of the specimen crystal as presented to the incident beam. It is easily shown that such findings are consistent with the presentation in Figs. 4 and 5.

Another way in which we can check on our understanding of the local mosaic distributions involved for the chosen orientation(s) of the specimen crystal is to carry out (in the $+2\theta$ region) a 180° rotation in the diffractometer angle χ and, if the crystal is not oriented in a symmetric position, change ω to $2\theta - \omega$. This procedure represents a change from the reflection *hkl* at ψ to the Friedel-pair reflection, $\bar{h}\bar{k}\bar{l}$, at $180° - \psi$ and is simulated by Figs. 5(*a*)(vii) and (ix), or (viii) and (x). Fig. 7 shows the $I(\Delta\omega, \Delta 2\theta)$ distribution obtained for the 112 reflection at $\psi = 260°$, *i.e.* the operation described above was carried out with the specimen crystal initially in the orientation which yielded Fig. 3(*a*)(ii). Fig. 7 is clearly in accord with Fig. 5(*b*)(ix), as expected, since Fig. 3(*a*)(ii) has already been shown to be compatible with Fig. 5(*b*)(vii). Similarly, when the operation described above is applied to the specimen crystal initially in the orientation that yielded Fig. 3(*a*)(i), the resulting $I(\Delta\omega, \Delta 2\theta)$ distribution is in accord with Fig. 5(*b*)(x).

3. Mosaic distribution about the scattering vector

In the various examples considered so far, for the 112 and $\bar{1}\bar{1}2$ reflections, Figs. 1(*b*), 3, 6 and 7, we have looked at essentially the same 'set' of local mosaic distributions along the crystal, but it has been reoriented, relative to the incident X-ray beam, within the diffraction plane. If we investigate a different region of the specimen crystal, by changing the reflection under consideration or by rotating about the scattering vector (by an amount other than 180°), we may well observe a different 'set' of local mosaic distributions along the crystal [*e.g.* see Figs. 1(*a*) and 2], owing to the inhomogeneous nature of the general mosaic distribution for the specimen crystal.

As an example of the way in which the mosaic distribution seen in the diffraction plane can change with specimen-crystal orientation, $I(\Delta\omega, \Delta 2\theta)$ distributions were recorded at several positions about the scattering vectors of the 112 and $\bar{1}\bar{1}2$ reflections. Rather than try to present all the information contained in these data, we have chosen to display one particular aspect of the mosaic distributions, namely the asymmetry and angular width. Figs. 8(*a*) and (*b*)

show polar plots of the distances, along $\Delta\omega^{(0)}$,* from the Mo $K\alpha_1$ peak position to the 10% contour, as a function of ψ, for the 112 and $\bar{1}\bar{1}\bar{2}$ reflections respectively. The distance from the peak position in the $+\Delta\omega^{(0)}$ direction is plotted toward the value of ψ concerned in each case, and the distance in the $-\Delta\omega^{(0)}$ direction in the opposite direction. The curves in Figs. 8(a) and (b), representing only a 180° rotation in ψ, are actually plotted by averaging the distances from the peak position, in the $+\Delta\omega$ direction for ψ and in the $-\Delta\omega$ direction for $180°+\psi$. These pairs of distances were always approximately equal [see Fig. 5(b)], with existing differences being largely attributable [with reference to the actual $I(\Delta\omega, \Delta 2\theta)$ distributions] to the intrinsically greater extent, along $\Delta\omega$, of $I(\Delta\omega, \Delta 2\theta)$ distributions like Figs. 5(b)(vii) and (ix), as opposed to those like Figs. 5(b)(viii) and (x).

* In cases where the $I(\Delta\omega, \Delta 2\theta)$ distribution 'leaned' away from the $\Delta\omega$ axis, due to non-parallel local mosaic spread centres, these distances were measured to the extremes of the 10% contour, as projected onto the $\Delta\omega$ axis.

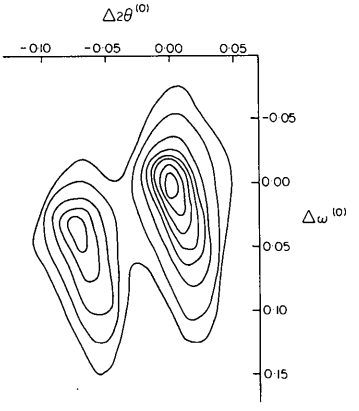

Fig. 6. The $I(\Delta\omega, \Delta 2\theta)$ distribution ($s=0$) obtained for the 112 reflection in the -2θ region at a value of ψ such that the crystal orientation is related to that for Fig. 3(a)(i) in the same way as the two crystal orientations used to get Fig. 2. The contour levels are the same as in Fig. 2.

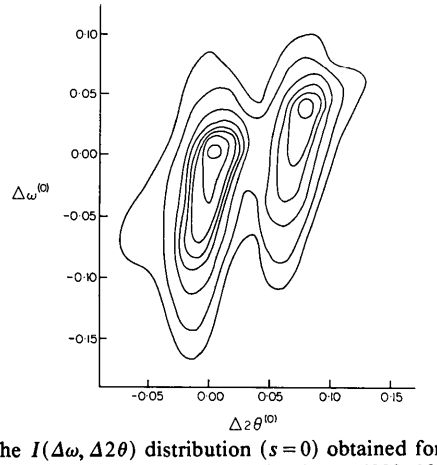

Fig. 7. The $I(\Delta\omega, \Delta 2\theta)$ distribution ($s=0$) obtained for the 112 reflection at $\psi=260°$. The contour levels are 4000, 3000, 2000, 1500, 1000, 500, 200 and 100 counts s^{-1}.

It is quite clear that there is a mirror relationship, in the horizontal line between 0 and 180° ψ, between Figs. 8(a) and (b). The reason for this is quite apparent from a consideration of the relationship between Figs. 5(b)(vii) and (ix), or (viii) and (x), as discussed at the end of § 2. The asymmetry (or, more

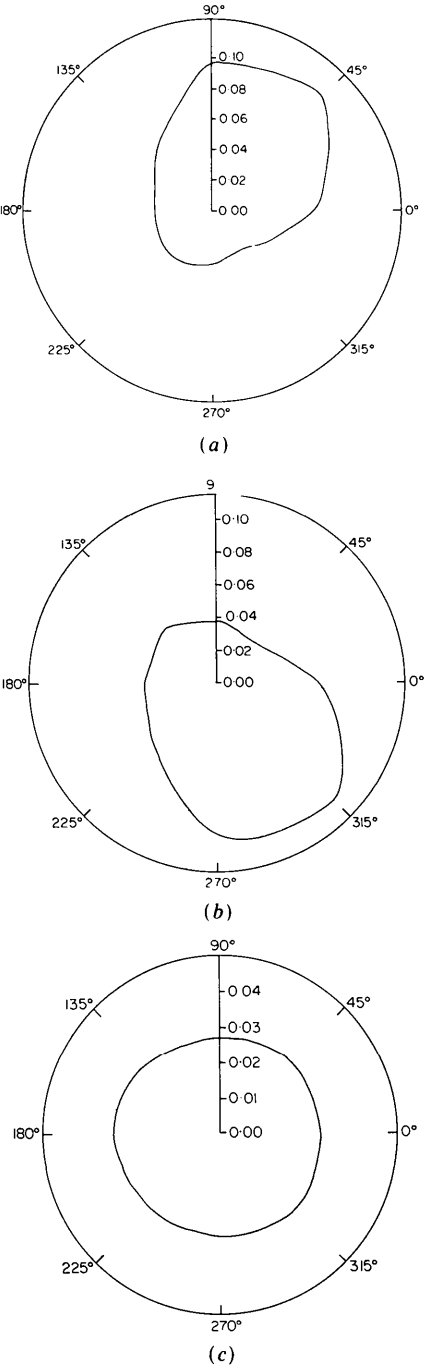

Fig. 8. Polar plots of the distances, along $\Delta\omega^{(0)}$, from the Mo $K\alpha_1$ peak position to the 10% contour as a function of ψ, for (a) the 112 reflection and (b) the $\bar{1}\bar{1}\bar{2}$ reflection. Further details are given in the text. (c) Polar plot analogous to Fig. 8(a), but in relation to $\Delta 2\theta$ rather than $\Delta\omega$.

specifically, the positions of the extremes of the 10% contour, as projected onto the $\Delta\omega$ axis, relative to the peak position) for the 112 reflection at a position ψ will be of essentially the same magnitude, but of the opposite sense, as that for the $\bar{1}\bar{1}2$ reflection at $180°-\psi$, and therefore the same (in both magnitude and sense) as that *indicated* for the $\bar{1}\bar{1}2$ reflection at $-\psi$ (hence the mirror).

In Fig. 8(*a*) [(*b*)], the narrowest part is (roughly) along the line from 135 to 315° [45 to 225°] and the widest part is along the line 90° away, *i.e.* from 45 to 225° [135 to 315°]. In each case, the narrowest part of the figure (through the pole) is also the most symmetrical, and the widest part is also the most asymmetrical. These observations are entirely consistent, for example, with the findings of Duisenberg (1983), who treated 'anisotropic mosaicity and splitting' of crystals by means of a 'rotational cluster model'. In the present case, and in the parlance of Duisenberg (1983), the neat profiles for the 112 and $\bar{1}\bar{1}2$ reflections would be at azimuthal angles (ψ_0) of approximately 135 (or 315) and 45° (or 225°) respectively. In discussing Figs. 8(*a*) and (*b*) in relation to Duisenberg's (1983) findings, it should be stated that, although his work is in relation to conventional one-dimensional intensity profiles and Figs. 8(*a*) and (*b*) depict results from what are essentially slice scans, a comparison is still valid, at least in this case, because the 'slice scans' are representative of the conventional intensity profiles that would be derived. That is, the narrowest and most symmetrical intensity profiles do occur at approximately the azimuthal angles mentioned above, as do the widest and most asymmetrical profiles. It should be noted however that the widest intensity profiles in the present case are narrower, by approximately an order of magnitude, than those of Duisenberg (1983) and are only representative of what he calls 'anisotropic mosaicity' and not 'splitting' of the specimen crystal.

Fig. 8(*c*) shows a polar plot analogous to Fig. 8(*a*), but in relation to $\Delta 2\theta$ rather than $\Delta\omega$. In Figs. 8(*a*) and (*b*) the major contribution was from μ, whereas this component, being at right angles to the $\Delta 2\theta$ axis for the $s=0$ scan mode, makes no contribution to Fig. 8(*c*) (see Mathieson, 1984*c*). The variation observed in Figs. 8(*a*) and (*b*) is due to the variation in μ with ψ. As in Figs. 8(*a*) and (*b*), the contributions from σ, λ and c remain constant in Fig. 8(*c*).* Hence, Fig. 8(*c*) is, to a good approximation, a circle centred on the pole. The contribution of the σ component to the diameter of Fig. 8(*c*) is, for a source-to-crystal distance S of ~214 mm, a take-off angle of 4° and a 0·4 mm wide X-ray focus (as viewed down the length of the tube), $(0{\cdot}4\tan 4°/214)(180°/\pi)\simeq 0{\cdot}007°$. The contribution of the λ component is given by $2(\Delta\lambda/\lambda)\tan\theta$ (see Mathieson, 1984*c*). If we assume that the shape of the Mo $K\alpha_1$ peak can be described by $I=I_0/[1+4(\lambda-\lambda_0)^2\mathrm{FWHH}^{-2}]$, where I_0 and λ_0 are the intensity and wavelength respectively at the maximum (Hoyt, 1932), the width at the 10% level is $3\mathrm{FWHH}\simeq 0{\cdot}9$ mÅ (Compton & Allison, 1935). The λ contribution is thus $2(0{\cdot}0009/0{\cdot}7093)\tan 6{\cdot}1° \times(180°/\pi)\simeq 0{\cdot}016°$. The c contribution can be shown to be $a_c(1+S\cos 2\theta/D)$, where a_c is the angle subtended by the crystal at the source, in the diffraction plane [*cf.* Mathieson (1984*a*, *c*) for the $S=D$ case]. This amounts to $(0{\cdot}06/214)(180°/\pi)(1+214\cos 12{\cdot}2°/252)\simeq 0{\cdot}029°$. Finally, the contribution due to the width of the detector aperture (~0·1 mm) is $(0{\cdot}1/252)(180°/\pi)\simeq 0{\cdot}023°$, giving a total figure of 0·075° for the predicted diameter of Fig. 8(*c*). This is in reasonable agreement with Fig. 8(*c*), where the diameter ranges from ~0·055 to ~0·058°.

4. Discussion

The analysis of the $I(\Delta\omega, \Delta 2\theta)$ distributions collected with the improved technique (Mathieson & Stevenson, 1984, 1985) has revealed that one can learn a great deal about the mosaic spread along the projected length of a quite small crystal in respect of a particular orientation (in the diffraction plane). The comparison of such distributions, collected for closely related crystal orientations, has confirmed the interpretation of the results.

The importance of the improved $\Delta\omega, \Delta 2\theta$ technique, whereby the σ component is reduced to a minor angular role, is more fully appreciated when it is realized that those characteristics of Figs. 3, 6 and 7 associated with the asymmetry and inhomogeneity of the local mosaic spreads and the non-parallelism of the distribution centres along the crystal cannot be detected in the corresponding $I(\Delta\omega, \Delta 2\theta)$ distributions collected with a 'short' source (Mathieson & Stevenson, 1984), let alone the conventional one-dimensional intensity profiles, $I(\Delta\omega)$.

The fact that the $\Delta\omega, \Delta 2\theta$ technique employed here is capable of identifying diffraction from one side of the specimen crystal to the other (in the diffraction plane), even for very small crystals, indicates that the shape and size of the specimen are of importance, in particular, in regard to the extent of the intensity distribution in $\Delta 2\theta$.

The establishment of a technique capable of showing the intricacies of the μ distribution for particular Bragg reflections (including equivalents) could lead, because of the intimate relationship between μ and the reflectivity r (or 'level of interaction'), to a more

* For c this is only an approximation. In the cases under consideration here, the 112 and $\bar{1}\bar{1}2$ reflections, the size of the crystal as presented to the incident X-ray beam in the diffraction plane changes little for rotations in ψ.

accurate prescription for structure-factor estimation (Mathieson, 1979, 1984*b*).

The small $CuInSe_2$ single crystal used in this study has proved to be a convenient, but in no way special, specimen with which to demonstrate some of the possibilities of the $\Delta\omega, \Delta 2\theta$ technique. The experimental observations have general significance for the modelling of crystals, since such models are mostly based on homogeneous mosaic spread (by contrast see Boehm, Prager & Barnea, 1974; Le Page & Gabe, 1978). The characteristics of the local mosaic distributions have proved to be quite diverse, even for the limited number of aspects in which the crystal has been viewed. Clearly, further work, with a variety of crystal specimens, is required to realize and appreciate the full potential of this technique.

One of us (AWS) acknowledges the financial support of a CSIRO Postdoctoral Award.

Note added in proof: A more accurate estimate of the diameter of Fig. 8(*c*) (see the end of § 3) can be obtained by carrying out a two-dimensional convolution of the functional forms associated with (μ), σ, λ, c and the detector aperture, *i.e.* a simulation of an $I(\Delta\omega, \Delta 2\theta)$ distribution. Such a calculation yields a value of ~0·051°.

References

BOEHM, J. M., PRAGER, P. R. & BARNEA, Z. (1974). *Acta Cryst.* A**30**, 335-337.

COMPTON, A. H. & ALLISON, S. K. (1935). *X-rays in Theory and Experiment.* New York: Van Nostrand.

DUISENBERG, A. J. M. (1983). *Acta Cryst.* A**39**, 211-216.

HOYT, A. (1932). *Phys. Rev.* **40**, 477-483.

LE PAGE, Y. & GABE, E. J. (1978). *J. Appl. Cryst.* **11**, 254-256.

MATHIESON, A. MCL. (1979). *Acta Cryst.* A**35**, 50-57.

MATHIESON, A. MCL. (1982). *Acta Cryst.* A**38**, 378-387.

MATHIESON, A. MCL. (1984*a*). *J. Appl. Cryst.* **17**, 207-209.

MATHIESON, A. MCL. (1984*b*). *Acta Cryst.* A**40**, 355-363.

MATHIESON, A. MCL. (1984*c*). *Aust. J. Phys.* **37**, 55-61.

MATHIESON, A. MCL. & STEVENSON, A. W. (1984). *Aust. J. Phys.* **37**, 657-665.

MATHIESON, A. MCL. & STEVENSON, A. W. (1985). *Acta Cryst.* A**41**, 290-296.

PARKES, J., TOMLINSON, R. D. & HAMPSHIRE, M. J. (1973). *J. Appl. Cryst.* **6**, 414-416.

Acta Cryst. (1986). A**42**, 230-240

On Absolute Scaling in Protein Crystallography using Sums of Low-Resolution Intensities and Wilson Statistics at Low Resolution

BY MICHEL ROTH

Institut Laue-Langevin, 156*X*, 38042 *Grenoble CEDEX, France*

(*Received* 11 *July* 1985; *accepted* 23 *December* 1985)

Abstract

A method of absolute scaling of diffraction data is proposed, based on the calculation of the sum of the intensity diffracted at low resolution (Bragg d spacing >15 Å). This sum is proportional to the mean-square deviation of the scattering-length density in the unit cell, and this property is used to determine the scale factor. The method is applied to the case of neutron diffraction using contrast variation experiments with biological molecules, and it is used to check the validity of some assumptions concerning the system under study, such as the global rate of H/D exchange or the uniformity of scattering-length density in the molecules. The use of this method requires an asymptotic correction of the sum of intensity. This correction is based on Porod's law, whose application to diffraction experiments is discussed, in particular for contrast variation experiments. An analysis of the spherical average of the diffracted intensity as a function of the scattering vector, compared to isotropic solution scattering, allows the conditions of applicability of Wilson statistics to be specified at low and medium resolution, *i.e.* the random statistical model underlying the Wilson statistics in this scattering range to be defined.

1. Introduction

In a structural study of complex molecules, such as biological macromolecules, by low-resolution neutron crystallography using H_2O/D_2O contrast variation, it is essential to know all the data concerning the contrast of all components of the system accurately. In practice, these values are usually calculated from the available information on the chemical composition of the components, making assumptions on the degree of H/D exchange on different sites within the components. Looking for a simple method

0108-7673/86/040230-11$01.50